Impedance-Model-Based MIMO Analysis of Power Synchronization Control

Javad Khazaei, *Member, IEEE,* Zhixin Miao, *Senior Member, IEEE,* and Lakshan Piyasinghe

***Abstract*—This paper presents impedance-model-based stability analyses of power synchronization control (PSC) and two types of vector controls used in voltage source converter-based high voltage direct current (VSC-HVDC) systems. The impedance model of a VSC with PSC is first derived. Stability analysis is then carried out using multi-input multi-output (MIMO) system analysis. As a comparison, power and angle transfer function-based analysis is also conducted. The impedance model-based stability analysis results are validated by the time-domain simulations. Impedance models of two types of vector controls are also derived for comparison. Effects of short circuit ratio (SCR), power transfer level, high-pass filters, and the PSC gain are demonstrated through analysis and real-time digital simulations in RT-LAB.**

***Index Terms*—power synchronization control, vector control, weak ac system, Nyquist stability criterion, impedance model.**

I. Introduction

Conventional line current commutating converter (LCC)-HVDC transmission systems cannot perform properly if the interconnected ac system is not strong enough [1–3]. The strength of an ac system is commonly defined by short circuit ratio (SCR), which depends on the HVDC nominal power and the strength of the ac system. Normally, systems with SCR values of less than 1.5 are considered as weak ac systems [4–6]. In contrast to the traditional HVDC systems, VSC-HVDC can be connected to very weak ac systems without any reactive compensation [7]. Vector current control is the most popular control scheme for the VSC-HVDC systems [8, 9]. Vector control of the VSC-HVDC can control the converters in weak ac systems with independent active and reactive power support to the grid [10, 11].

However, there are some barriers regarding the application of vector control especially when a VSC is connected to a very weak ac system. Studies have shown that vector current control of a VSC-HVDC cannot transfer power levels of more than 0.4 p.u once connected to a grid with the SCR level of 1 [12, 13]. Analytical studies indicated that the limiting factors of vector controls can be the interactions between current controls and grid inductances [6, 14] and/or phase-locked-loop (PLL) dynamics [6, 14, 15]. It is mentioned in [6, 14] that low frequency resonances may occur due to the interactions of vector current control and weak ac systems. Additionally, the PLL dynamics will cause problems when the converter is synchronized with the weak grid. To overcome the weak grid issue, [15] applied gain scheduling technique to design the outer loop power/voltage as an MIMO control system, which resulted in an increase in the power transfer level. Another solution is the power synchronization control (PSC) [13]. Compared to the gain scheduling control where the controller's gain varies, PSC serves as a classic type controller with a fixed structure and fixed parameters. The PSC has also been shown as a superior alternative for vector control of VSC-HVDC systems in connection to weak ac grids [13, 16–19]. Unlike the PLL that synchronizes the converter to the point of common coupling (PCC), the PSC directly synchronizes the converter to the grid through a power control loop.

Application of the PSC control method has been studied in a few papers. In the first paper [13], the power synchronization is introduced as an alternative to the conventional vector control in weak ac systems. In [16], the PSC is used to interconnect two very weak ac systems. The effect of different parameters on the stability of the system is also investigated. The application of the PSC for offshore wind farms is introduced in [17]. Stability limitations of various control loops in HVDC system enhanced with PSC are studied in [18]. It is found that alternating voltage controls make systems more stable compared to reactive power controls. Moreover, the impact of the converter with the PSC control on sub-synchronous resonance (SSR) damping is studied in [19], which shows that the PSC can greatly improve the damping for SSR modes.

In the original PSC paper, the power versus angle transfer function is used to carry out the stability analysis [13]. The power versus angle transfer function considers a single input single output (SISO) system, with the effect of voltage on active power ignored.

Impedance modeling is a popular approach for converter and grid interaction analysis [6, 20–23]. The impedance model of the PSC has been derived in [19] for a converter connected to a series compensated transmission line. The main focus of [19] is to study the effect of power synchronization control on sub-synchronous resonance caused by the interactions between the synchronous generator and the converter. The analysis in [19] relies on the frequency responses of the impedance matrices. MIMO system analysis techniques were not adopted in the aforementioned reference.

The main contribution of our paper is to analyze the stability and robustness of the PSC for a VSC-HVDC interconnected to a weak ac grid using impedance models. The MIMO system impedance is derived and system stability is then evaluated using singular value robustness analysis. Two types of vector controls are also considered for comparison. The impedance model of converters with vector control has been developed

J.Khazei is with the school of science, engineering, and technology (SSET) at Penn State Harrisburg, and Z. Miao, and L. Piyasinghe are with Department of Electrical Engineering at University of South Florida, Tampa, FL (Emails: jxk792@psu.edu; zmiao@usf.edu; lakshan@mail.usf.edu).

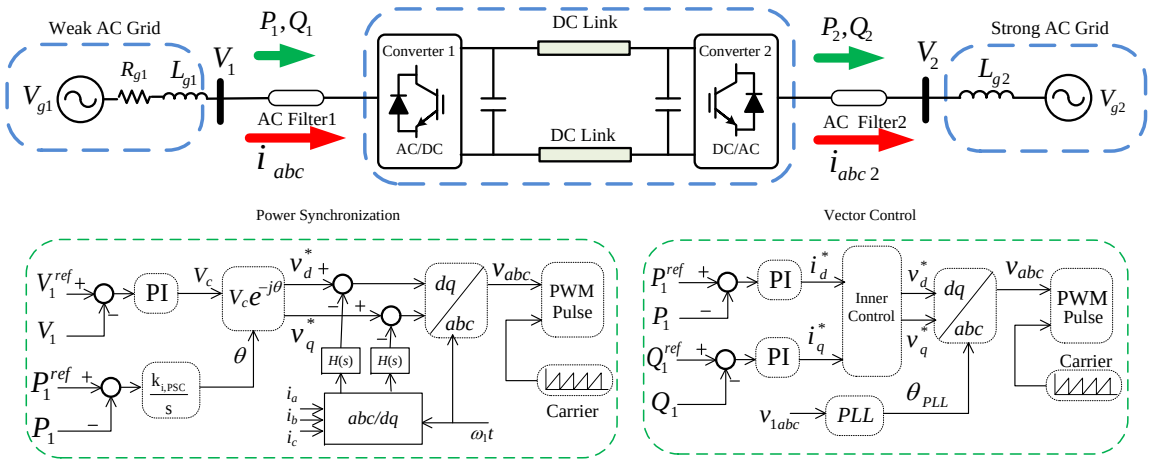

Fig. 1: Back-to-back VSC-HVDC connected to a weak ac system. Two different controls for the rectifier are also presented.

in the literature, as shown in [6, 14]. However, outer control loops have not been considered. In this study, comprehensive impedance models of vector controls will be derived for comparison purpose.

Nyquist theory and the singular value of the return matrix are applied for the stability and robustness analysis, respectively. The eigen loci of the open-loop system and singular value plots of the return difference matrix are employed in the MIMO stability analysis.

The circuit and control structure of the system is shown in Fig. 1. The PSC is implemented on the rectifier side of the VSC-HVDC system (Converter 1). For comparison, the impedance models for vector control of VSC-HVDC are also derived. Two types of vector controls (with and without power outer loops) will be examined.

The rest of the paper is organized as follows. Section II describes the small-signal models used to derive the impedance model. Section III presents the power/angle transfer function. Section IV presents MIMO system-based stability analysis and validation results by simulation. Section V concludes the paper.

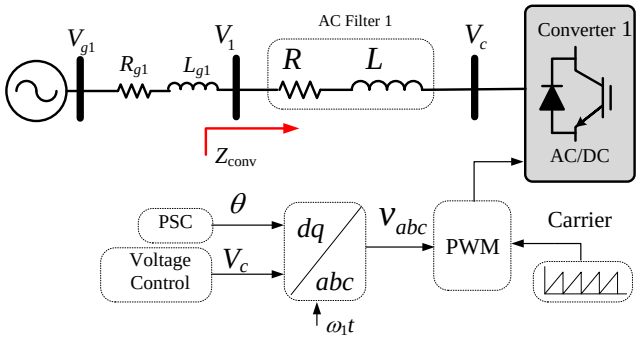

Fig. 2: Simplified model of the system with the PSC. The high-pass filters notated as $H(s)$ in Fig. 1 are omitted in this model. $R = 0\ \Omega$, $L = 0.04\ H$, $R_{g1} = 0.1\ \Omega$, $L_{g1} = 0.25$ H for $SCR = 1$, $L_{g1} = 0.088$ H for $SCR = 2$ and $L_{g1} = 0.048$ H for $SCR = 3$.

II. Small-Signal Model of the System

A. Circuit Dynamics

As the main contribution of this research is weak ac grids, the converter to be studied is the rectifier (Converter 1) that is connected to the weak ac grid. Fig. 2 illustrates a simple representation of the system in Fig. 1 with the rectifier converter, the ac grid and the filter considered. The high-pass filters notated in Fig. 1 as $H(s)$ are not included. $Z_g(s) = R_{g1} + sL_{g1}$ is the total impedance of the weak ac grid and its transformer, $Z_{\text{conv}}(s)$ is the impedance viewed from the point of common coupling (PCC). V_c is the converter input voltage and V_{g1} is the ac grid voltage. The ac filter is represented by R and L. As it can be observed, the converter is equipped with the PSC and an alternating voltage control. The main dynamics related to the inductor in the dq-reference frame (rotating at a synchronous speed ω_1) is expressed as:

$$\overline{V}_1 - \overline{V}_c = L\frac{d\overline{I}}{dt} + j\omega_1 L\overline{I} + R\overline{I}. \tag{1}$$

where, $\overline{V}_1$, $\overline{V}_c$, and $\overline{I}$ are complex vectors for the PCC voltage, the converter voltage, and the line current i_{abc} in the dq-reference frame. $\overline{V}_1 = v_{1d} + jv_{1q}$, $\overline{V}_c = v_{cd} + jv_{cq}$, and $\overline{I} = i_d + ji_q$.

Further, the converter input voltage is defined using its magnitude V_c and the angle relative to the dq-reference frame $-\theta$ based on the PSC control in Fig. 1:

$$\overline{V}_c = V_c e^{-j\theta} = V_c\cos(\theta) - jV_c\sin(\theta) \tag{2}$$

where θ is the output from the power control.

Since $\overline{V}_c = V_c e^{-j\theta}$, therefore its small-signal expression is

$$\begin{aligned}\Delta\overline{V}_c &= -jV_{c0}e^{-j\theta_0}\Delta\theta + e^{-j\theta_0}\Delta V_c \\ &= -j\overline{V}_{c0}\Delta\theta + e^{-j\theta_0}\Delta V_c.\end{aligned} \tag{3}$$

where the subscript $_0$ represents initial condition.

In Laplace domain, we now have:

$$\begin{aligned}\Delta\overline{I} &= \frac{\Delta\overline{V}_1 - \Delta\overline{V}_c}{R + (s + j\omega_1)L} \\ &= \frac{\Delta\overline{V}_1 + j\overline{V}_{c0}\Delta\theta - e^{-j\theta_0}\Delta V_c}{R + (s + j\omega_1)L}.\end{aligned} \tag{4}$$

$$\underbrace{\begin{bmatrix}\Delta i_d\\ \Delta i_q\end{bmatrix}}_{I(s)} = \underbrace{\frac{\begin{bmatrix}R+sL & \omega_1 L\\ -\omega_1 L & R+sL\end{bmatrix}}{(R+sL)^2+(\omega_1 L)^2}}_{G_{11}} \underbrace{\begin{bmatrix}\Delta v_{1d}\\ \Delta v_{1q}\end{bmatrix}}_{V_1(s)} + \underbrace{\frac{\begin{bmatrix}\omega_1 L v_{cd0}-(R+sL)v_{cq0}\\ (R+sL)v_{cd0}+\omega_1 L v_{cq0}\end{bmatrix}}{(R+sL)^2+(\omega_1 L)^2}}_{G_{12}}\Delta\theta + \underbrace{\frac{\begin{bmatrix}\omega_1 L\sin\theta_0-(R+sL)\cos\theta_0\\ \omega_1 L\cos\theta_0+(R+sL)\sin\theta_0\end{bmatrix}}{(R+sL)^2+(\omega_1 L)^2}}_{G_{13}}\Delta V_c \quad (5)$$

Separating into dq components, we now have the small-signal model of the circuit dynamics in (5).

B. Power Synchronization Control

The key structure of the PSC is illustrated in Fig. 1. The idea behind the PSC comes from the analogy of the power and angle relationship in synchronous machines [13]. In the PSC, synchronization takes place by controlling the active power through the converter. The PSC output is then used as the reference angle for the VSC PWM unit. By applying this method, the PLL is not needed. Referring to Fig. 1, the difference between the reference active power of the converter and the measured power is sent to an integrator controller ($\frac{K_{i,\mathrm{PSC}}}{s}$), and the output of which presents the synchronization angle (θ) [13].

$$\theta(s) = \frac{K_{i,\mathrm{PSC}}}{s}(P_1^{\mathrm{ref}}(s) - P_1(s)) \quad (6)$$

The complex power from the PCC bus to the converter is notated as S_1: $S_1 = \overline{V}_1\overline{I}^* = (v_{1d}+jv_{1q})(i_d - ji_q)$.

The small-signal equations of active and reactive power are as follows:

$$\begin{aligned}\Delta P_1 &= \Delta v_{1d} i_{d0} + \Delta i_d v_{1d0} + \Delta v_{1q} i_{q0} + \Delta i_q v_{1q0},\\ \Delta Q_1 &= \Delta v_{1q} i_{d0} + \Delta i_d v_{1q0} - \Delta v_{1d} i_{q0} - \Delta i_q v_{1d0}.\end{aligned} \quad (7)$$

Therefore, the small-signal representation of the power synchronization loop is derived by obtaining the small-signal model of (6) and replacing ΔP_1 using (7):

$$\Delta\theta = \underbrace{-\frac{K_{i,\mathrm{PSC}}}{s}\begin{bmatrix}i_{d0}\\ i_{q0}\end{bmatrix}^T}_{G_{21}}\begin{bmatrix}\Delta v_{1d}\\ \Delta v_{1q}\end{bmatrix} \underbrace{-\frac{K_{i,\mathrm{PSC}}}{s}\begin{bmatrix}v_{1d0}\\ v_{1q0}\end{bmatrix}^T}_{G_{22}}\begin{bmatrix}\Delta i_d\\ \Delta i_q\end{bmatrix} + \frac{K_{i,\mathrm{PSC}}}{s}\Delta P_1^{\mathrm{ref}} \quad (8)$$

C. AC Voltage Control Loop

As illustrated in Fig. 1, the AC voltage controller regulates the magnitude of the rectifier voltage to maintain the grid side voltage. A simple PI controller is used to control the magnitude of the voltage, and the output of which is employed to generate the reference converter voltage magnitude V_c. Dynamic equation for the alternating voltage controller can be expressed by [19]:

$$V_c = \left(k_{pv} + \frac{k_{iv}}{s}\right)(V_1^{\mathrm{ref}} - V_1). \quad (9)$$

where V_1^{ref} is the reference magnitude of the PCC voltage, and V_1 is the measured magnitude of PCC voltage, $\sqrt{v_{1d}^2+v_{1q}^2}$.

Therefore, the small-signal representation of V_1 can be represented by:

$$\Delta V_1 = \frac{1}{V_1}(v_{1d0}\Delta v_{1d} + v_{1q0}\Delta v_{1q}) \quad (10)$$

Applying the small-signal analysis to (9) and replacing ΔV_1 in (9) by (10) leads to:

$$\Delta V_c = \left(k_{pv}+\frac{k_{iv}}{s}\right)\Delta V_1^{\mathrm{ref}} \underbrace{-\left(k_{pv}+\frac{k_{iv}}{s}\right)\begin{bmatrix}\frac{v_{1d0}}{V_1}\\ \frac{v_{1d0}}{V_1}\end{bmatrix}^T}_{G_3}\begin{bmatrix}\Delta v_{1d}\\ \Delta v_{1q}\end{bmatrix} \quad (11)$$

Parameters of the PSC are included in the Table III of the Appendix.

D. Impedance Model of a VSC with PSC Control

Finally, the block diagram considering the circuit dynamics in (5), PSC in (8), and voltage control in (11) is presented in Fig. 3.

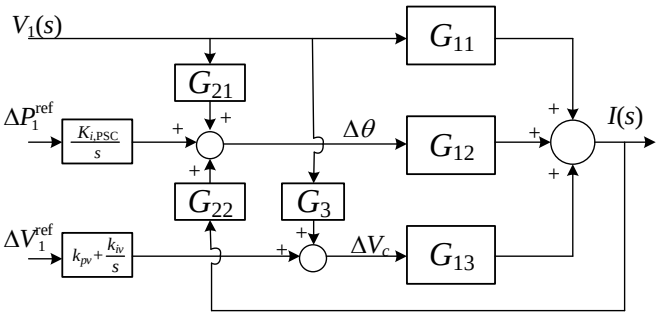

Fig. 3: Block diagram consisting the circuit dynamics, PSC, and voltage control.

The relationship between the inputs and outputs is as follows:

$$I(s) = \underbrace{(I - G_{12}G_{22})^{-1}(G_{11} + F_{12}G_{21} - G_{13}G_3)}_{Y_{\mathrm{conv}}}V_1(s) + \underbrace{(I - G_{12}G_{22})^{-1}\begin{bmatrix}\frac{K_{i,\mathrm{PSC}}}{s}G_{12}\\ \left(k_{pv}+\frac{k_{iv}}{s}\right)G_{13}\end{bmatrix}^T\begin{bmatrix}\Delta P_1^{\mathrm{ref}}\\ \Delta V_1^{\mathrm{ref}}\end{bmatrix}}_{-I_c} \quad (12)$$

where I is a 2×2 identity matrix. This notation should be differentiated from $I(s)$, the current vector's Laplace form.

Y_{conv} is the admittance model of the converter and the impedance model Z_{conv} is the inverse of the admittance matrix: $Z_{\mathrm{conv}} = Y_{\mathrm{conv}}^{-1}$. It can be seen that the impedance model is also a 2×2 matrix.

Equation (12) describes a Norton equivalent of the converter with the RL filter. The entire system in Fig. 2 can now be expressed as a circuit in Fig. 4.

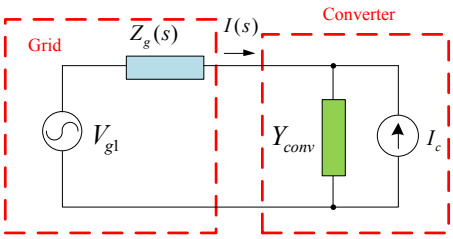

Fig. 4: Impedance model of a converter connected to a grid.

III. Transfer Function-based analysis

Given the power control loop, it is easy to seek the relationship between the complex power $S_c = P_c + jQ_c$ injected to the converter versus the voltage magnitude V_c and the angle θ. The following derivation is based on small-signal model of the complex power in the dq reference frame. Our derivation is based on the complex power definition and line impedance model. Compared to the derivation in [13], the following derivation is straightforward and easy to follow. If R is ignored, then $P_1 = P_c$.

In the dq-reference frame, the complex vectors of the converter voltage and the grid voltage are as follows:

$$\overline{V_c} = V_c \angle -\theta, \quad \overline{V}_{g1} = V_{g1} \angle 0 \tag{13}$$

where V_{g1} is assumed to be constant, while V_c and θ are controlled through the PSC's voltage and power controls.

The electromagnetic dynamics of the line will not be neglected. As a result, in Laplace domain, the current and voltage relationship in the dq reference frame is

$$\overline{I}(s) = \frac{\overline{V}_{g1}(s) - \overline{V}_c(s)}{\widetilde{R} + (s + j\omega_1)\widetilde{L}}. \tag{14}$$

where $\widetilde{R}$ and $\widetilde{L}$ are the total resistance and inductance between the grid and the converter. Note that the line impedance model in abc reference frame is $\widetilde{R} + s\widetilde{L}$, while in a synchronous reference frame it becomes $\widetilde{R} + (s + j\omega_1)\widetilde{L}$.

The small-signal model of (14) is also derived as follows. Assuming that the grid voltage is constant, then $\Delta\overline{V}_{g1} = 0$.

Therefore,

$$\Delta\overline{I}(s) = \frac{j\overline{V}_{c0}\Delta\theta - e^{-j\theta_0}\Delta V_c}{\widetilde{R} + (s + j\omega_1)\widetilde{L}}. \tag{15}$$

Since the complex power to the converter can be expressed as $S_c = \overline{V}_c\overline{I}^*$, its expression in Laplace domain will be:

$$\Delta S_c(s) = \overline{V}_{c0}\Delta\overline{I}^*(s) + \overline{I}_0^*\Delta\overline{V}_c(s) \tag{16}$$

where the subscript 0 notates the initial conditions.

Substituting $\Delta\overline{I}(s)$ using (15) and substituting $\Delta\overline{V}_c$ using (3), we have

$$\Delta S_c = \begin{bmatrix} \frac{j\overline{V}_{c0}^2}{\widetilde{R}+(s-j\omega_1)\widetilde{L}} - jS_{c0} \\ \frac{-\overline{V}_{c0}}{R+(s-j\omega_1)L} - \overline{I}_0^* e^{-j\theta_0} \end{bmatrix}^T \begin{bmatrix} \Delta\theta(s) \\ \Delta V_c(s) \end{bmatrix} \tag{17}$$

where S_{c0} is the initial complex power and $S_{c0} = \overline{V}_{c0}\overline{I}_0^*$.

Separating the real and imaginary parts, we can find $\Delta P_c = J_{P\theta}\Delta\theta + J_{PV}\Delta V_c$. The power to angle transfer function can be found as:

$$J_{P\theta} = Q_{c0} - \frac{\omega_1\widetilde{L}V_{c0}^2}{(\widetilde{R} + s\widetilde{L})^2 + (\omega_1\widetilde{L})^2} \tag{18}$$

where Q_{c0} is the initial reactive power injected into the converter and $Q_{c0} = \mathrm{Im}(S_{c0})$.

The above transfer function indicates that there are 60 Hz resonances due to the line electromagnetic dynamics. This phenomenon has been mentioned in [13] and a high-pass filter has been implemented to increase the damping for this oscillating mode. The control idea is to increase the total resistance by introducing a virtual resistance via a high-pass filter. The resulting power angle transfer function becomes:

$$J_{P\theta} = Q_{c0} - \frac{\omega_1\widetilde{L}V_{c0}^2}{(\widetilde{R} + H(s) + s\widetilde{L})^2 + (\omega_1\widetilde{L})^2} \tag{19}$$

where $H(s)$ is the transfer function of the high-pass filter.

The virtual resistance will provide damping at 60 Hz. A high pass filter will fulfill this task: $H(s) = \frac{0.5s}{s+40}$. The implementation of the filter should be in the dq reference frame with a constant rotating speed ω_1 as shown in Fig. 1. It can be seen that the PSC is coupled with the AC grid and a high-pass filter is necessary. On the other hand, the vector control is equipped with a feed forward compensation ([10], Chap 3, pg. 53). The feedforward compensation decouples the converter operation from the grid and enhances the disturbance rejection capability. Therefore, there is no need for the high pass filter in the vector control based converters.

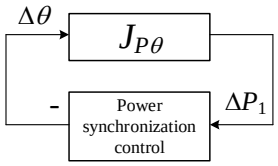

Fig. 5: The closed-loop system that consists of the PSC control and the plant model.

Remarks: If we ignore the voltage control's impact, we may have a closed-loop system shown in Fig. 5 with the PSC control and the plant model represented by (19). The open-loop transfer function is $\frac{K_{i,\mathrm{PSC}}}{s}J_{P\theta}$. Note that stability analysis in [13] is based on this system.

IV. MIMO Stability Analysis and Validation through Time-Domain Simulation

According to Fig. 4, the current can be derived as follows.

$$\begin{aligned} I(s) &= (Z_g + Z_{\mathrm{conv}})^{-1}(V_{g1}(s) - Z_{\mathrm{conv}}I_c(s)) \\ &= (Z_g + Z_{\mathrm{conv}})^{-1}Y_{\mathrm{conv}}^{-1}Y_{\mathrm{conv}}(V_{g1}(s) - Z_{\mathrm{conv}}I_c(s)) \\ &= [Y_{\mathrm{conv}}Z_g + Y_{\mathrm{conv}}Z_{\mathrm{conv}}]^{-1}Y_{\mathrm{conv}}(V_{g1}(s) - Z_{\mathrm{conv}}I_c(s)) \\ &= [I + Y_{\mathrm{conv}}Z_g]^{-1}(Y_{\mathrm{conv}}V_{g1}(s) - I_c(s)) \end{aligned} \tag{20}$$

where I is the identity matrix. For the above system, two assumptions are placed. (i) The grid voltage $V_{g1}(s)$ is stable;

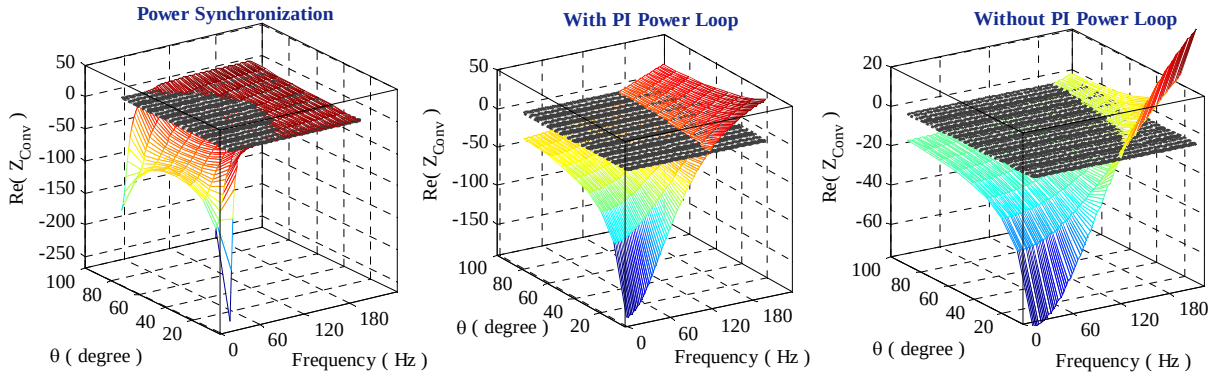

Fig. 6: Comparison between real parts of converter impedances, $Z_{\text{conv}}(j\omega)$'s first diagonal component for different controllers of rectifier side converter.

(ii) the current is stable when the grid impedance Z_g is zero, i.e., $Y_{\text{conv}}V_{g1}(s) - I_c(s)$ is stable. The first assumption is valid for the real-world scenarios as long as the grid voltage is within the limits. The second assumption is valid as long as the inverter converter admittance Y_{conv} is stable and current order is stable. For properly designed converters, the second assumption is also true. Therefore, for the current $I(s)$ to be stable, we only need to examine the denominator: $I + Y_{\text{conv}}(s)Z_g(s)$. In order to claim that the system is stable, the zeros or roots of the characteristic function $det(I + Y_{\text{conv}}(s)Z_g(s)) = 0$ should be located in the left half plane (LHP).

As both the grid and converter impedances are 2×2 matrices, the circuit analysis problem becomes a multi-input multi-output (MIMO) system stability problem. The MIMO system stability criterion is given in [24]. The characteristic function, $det(I + Y_{\text{conv}}Z_g) = 0$ should have no zeros in the RHP.

Such stability criterion can be examined by checking the eigen loci or the Nyquist plots of the eigenvalues of $Y_{\text{conv}}Z_g$. If the eigen loci do not encircle $(-1, 0)$, then the system is stable. This technique has been extensively used in the impedance-based stability analysis of the power electronic converters [14, 23]. On the other hand, the minimum singular value in the frequency domain of the return difference matrix $(I + Y_{\text{conv}}Z_g)$ provides an index of gain margin and phase margin [25]. The singular value plots have been adopted in the authors' previous publication [26] to conduct impedance-based stability analysis. The minimum singular value indicates how close the return difference matrix is to singularity or $det(I + Y_{\text{conv}}Z_g) \rightarrow 0$ at which frequencies. The greater the minimum singular value, the more robust the system. Resonance frequency can be identified as the frequency where the singular value is the minimum.

Results of the stability analysis will be validated by the high-fidelity model based simulation. The topology of the simulation model has been illustrated in Fig. 1 in detail. For the real-time simulation of the proposed system, RT-LAB is used. The detailed RT-LAB model includes pulse width modulation (PWM) switching details and dc system dynamics which can reflect the nonlinear and discrete behavior of the model. In addition to the PSC, two types of vector controls are designed for comparison. The first type has an outer active power and voltage control loop, an inner current control, and a PLL as shown in Fig. 1. The second type has no outer feedback loop. Instead, the current references are computed directly from power reference. This type of the vector control has been analyzed in [14] and the detailed vector control design and impedance derivation are presented in Appendices B and C.

To verify the strength of the system in analysis and simulation, three different SCR values are considered; $SCR = 1$ resembles a very weak ac system, $SCR = 2$ for a normal ac system, and $SCR = 3$ which is a strong system. The base values to calculate the SCRs are included below: $V_{\text{base}}(LL) = 100$ kV, $S_{\text{base}} = 100$ MVA, $P_{\text{HVDC}} = 100$ MVA, $L_{f1} = 0.04$ H, $L_{g1} = 0.25$ H for $SCR = 1$, $L_{g1} = 0.088$ H for $SCR = 2$ and $L_{g1} = 0.048$ H for $SCR = 3$.

A. Impedance of the Converter for Different Control

In the first case, impedances of the converter are derived for three separate controls. Fig. 6 shows the 3D diagonal (dd) component of $Z_{\text{conv}}(s)$ with the three controllers, where the gray surface is the surface where the real part of the impedance is zero. It is observed that with the PSC, the converter impedance is positive for the frequency ranges of more than 50 Hz for low power angles (or low power transfer level).

It is also noted that as the power angle (or power level) increases, the positive impedance occurs at a higher frequency. For instance, for the power angle of 80 degrees, the positive impedance happens at 70 Hz. Therefore, as the power level increases, the impendence becomes more negative at the fundamental frequency. Compared to the PSC, the vector control has negative impedance for frequency ranges of less than 120 Hz at low power angles. With an increase in the power angle (or power level), the impedance will be more negative. This shows that the PSC provides a positive impedance or more damping within the frequency ranges where the vector control provides a negative impedance.

B. Stability under Different SCR Scenarios

The first case study is designed to compare the PSC and two other types of vector control for systems with three different SCRs. The Nyquist plots for different controllers are illustrated

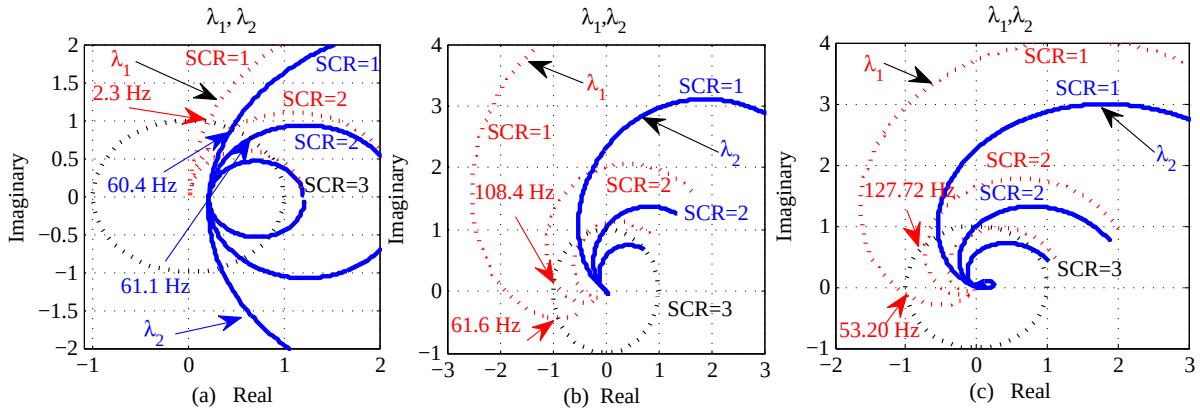

Fig. 7: Comparison of eigen loci of $Y_{\text{conv}}(j\omega)Z_g(j\omega)$ for different SCR values and controllers of the rectifier side converter. The power transfer level is 100 MW. The high pass filter is included for the PSC. (a) PSC; (b) vector control with PI power loop; (c) vector control without PI power loop.

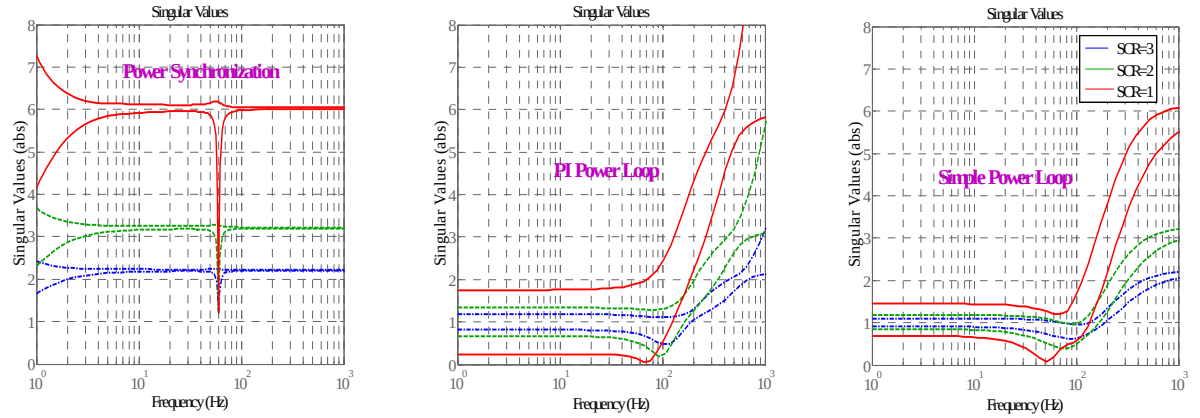

Fig. 8: Comparison of singular value plots of $I + Y_{\text{conv}}(s)Z_g(s)$ for the different SCR values and controllers of the rectifier side converter. The power transfer level is 100 MW.

in Fig. 7 and the singular plots for the return matrix are shown in Fig. 8.

Fig. 7 shows that for $SCR = 3$ none of the Nyquist plots encircle (-1,0) in a clockwise direction. All the control methods result in stable operation. When the SCR decreases, all of the controllers' performance deteriorates due to the reduction in the gain and phase margins as illustrated in Fig. 7. By decreasing the SCR to 1, the vector controls encircle the point $(-1, 0)$ in a clockwise direction, indicating instability. However, the PSC still provides a robust performance.

The singular value plots in Fig. 8 show that the PSC with the high pass filter has the minimum singular values greater than 1 for various SCR scenarios. This indicates a robust stability margin and immunity towards the SCR. On the other hand, the vector controls have the minimum singular values of less than 1. When the SCR reduces, this value also reduces, which indicates that the vector controls are prone to instability when the grid is weak. The singular value plots indicate that the resonance frequency in the dq-reference frame is 60 Hz for PSC. The eigen loci plots also indicate that the resonance frequency is around 60 Hz for one locus.

Simulation results for the vector control (with outer loop)

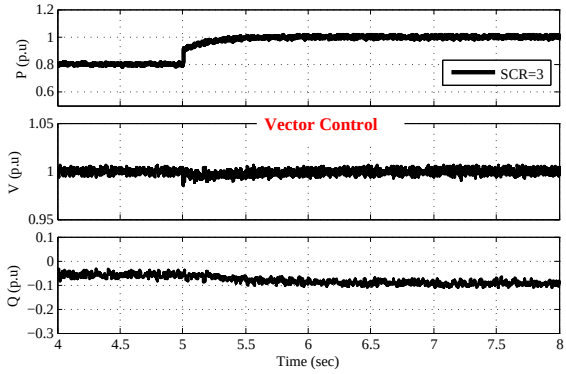

Fig. 9: Simulation results (real power, PCC voltage, and reactive power) for a step change in the real power when the vector control is applied and the SCR is 3.

are shown in Fig. 9 and Fig. 10. For the sake of simplicity, only two SCR values are included. The vector control aims to control the active power and terminal voltage at the rectifier station. The step reference power change is applied to change the reference power from 0.8 p.u to 1 p.u at the time 5 sec.

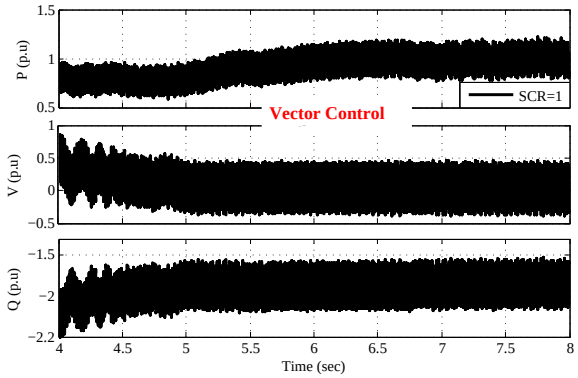

Fig. 10: Simulation results (real power, PCC voltage, and reactive power) for a step change in the real power when the vector control is applied and the SCR is 1.

It is observed that when the SCR is 3, the vector control can follow the reference active power step change. In contrast to the strong system, when the system is weak (SCR is 1) , the vector control fails to support the power transfer to 0.8 p.u. Simulation results are in agreement with the stability analysis illustrated in Figs. 7 and 8.

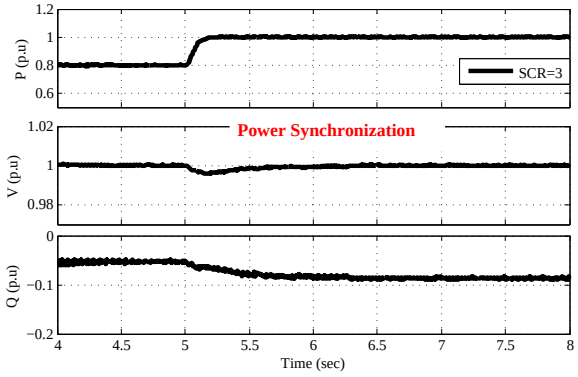

Fig. 11: Simulation results (real power, PCC voltage, and reactive power) for a step change in the real power when the PSC is applied and the SCR is 3.

Figs. 11-12 present the simulation results for the PSC in strong and weak ac grids. Same as the previous case, an active power change is applied to change the power transfer from 0.8 p.u. to 1 p.u. at 5 seconds. It is shown that for both cases, the system is stable and the PSC can successfully transfer the amount of active power which is needed. Compared to the vector control, the PSC can transfer 1 p.u. even in a very weak ac system connection.

Multiple power transfer levels for three separate controllers are presented in Fig. 13. The first figure is for the vector control with simple power controller. Compared to a simple power controller, the vector control with PI outer loop provides a better results for power levels of 80 MW and 100 MW. However, the vector control fails to transfer 150 MW in this case. In contrast, the PSC can transfer all three active power levels.

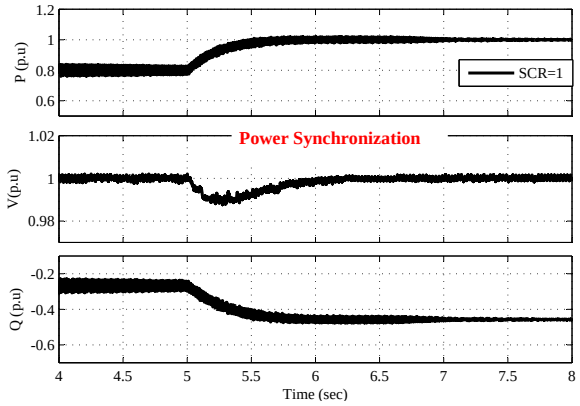

Fig. 12: Simulation results (real power, PCC voltage, and reactive power) for a step change in the real power when the PSC is applied and the SCR is 1.

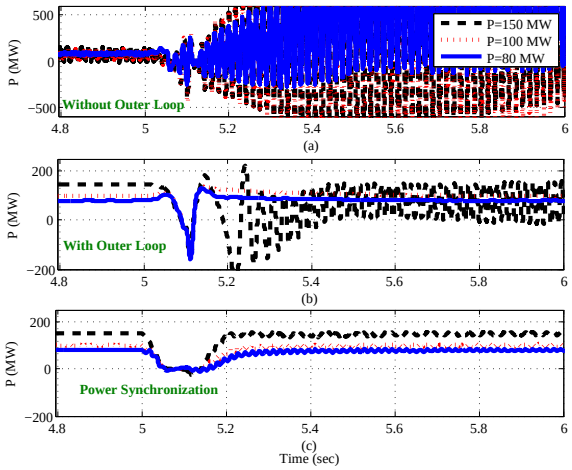

Fig. 13: Simulation results for different active power levels for three different control approaches. (a) Vector control without outer power loops. (b) Vector control with outer power loops. (c) Power synchronization control. A three-phase fault is applied at $t = 5$ s at the inverter ac side and cleared after one cycle. The SCR for this case is set to 2.

C. Effect of the High-Pass Filter

The effect of the high-pass filter is examined in this subsection. The studied filter will move the 60 Hz resonant poles to the left hand plane (LHP) and provide more stability margin to the PSC controller. The results of the root loci (on the open loop transfer function $J_{P\theta}\frac{K_{i,\mathrm{PSC}}}{s}$) comparison for two cases (with and without filters) are shown in Fig. 14. It is observed that by adding the filter, two resonant 60 Hz poles will move to the left in the s-plane, which indicates more damping.

Simulation results in Fig. 15 validate the analysis results. The system is simulated without the filter at the beginning and the filter is activated at 5 seconds. It is observed that after activating the filter, 60 Hz oscillations caused by resonant poles will be damped well.

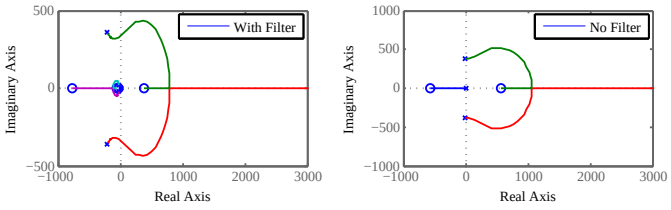

Fig. 14: Effect of filter on root locus curves of the system when SCR is 1.

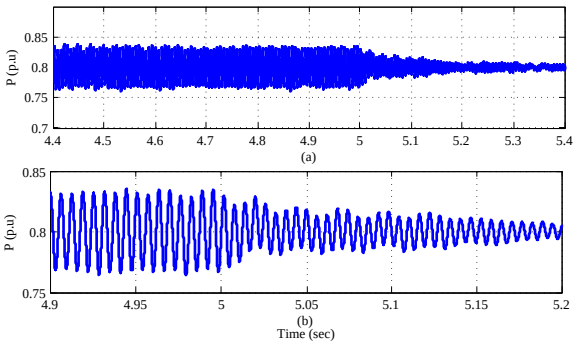

Fig. 15: Real-time simulation results for the effect of filter when SCR is 1 shown in different scales. (a) Effect of filter during the operation. (b) Zoom in version of the first subplot.

D. Effect of the PSC Loop Gain

A large PSC integral gain ensures a fast response. However, a large gain can result in instability. This issue was mentioned in [13] without presenting any analysis and simulation. In this subsection, the root loci of the open loop transfer function ($J_{P\theta}\frac{K_{i,\mathrm{PSC}}}{s}$) are used to indicate the range of $k_{i,\mathrm{PSC}}$.

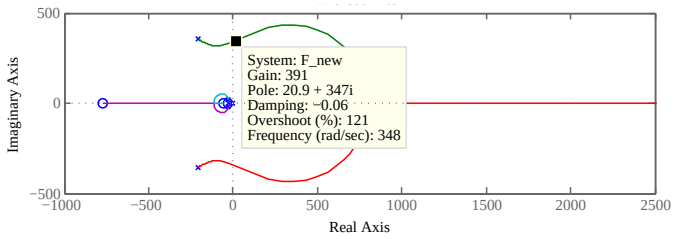

Fig. 16: Root loci of PSC for SCR equal to 1, with the high pass filter.

Results of root locus analysis of the system with PSC control are illustrated in Fig. 16. It is observed that by increasing the PSC gain to 390, the 60 Hz resonance poles will move to the right hand side of the s-plane and make the system unstable.

Simulation results for different PSC gains are presented in Fig. 17. When the PSC gain is set to 390, large oscillations are observed and power commands can not be followed. However, with the gain as low as 50, the system will be stable.

The developed impedance model is also used to investigate the effect of the filter and a large PSC gain. Fig. 18 shows the effect of the filter and large gain on singular value plots. The findings verify that the high-pass filter application helps to improve the minimum singular value. On the other hand, when

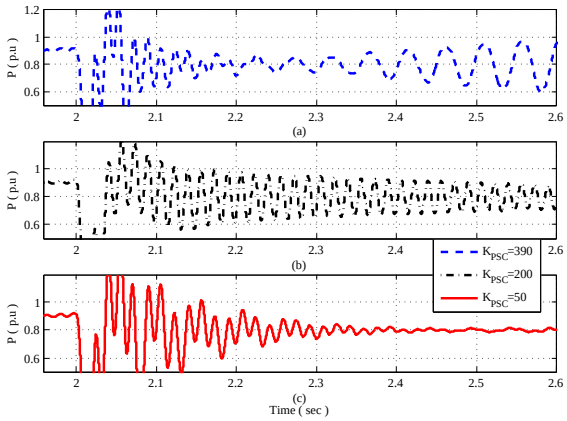

Fig. 17: Real-time simulation results for different PSC gain loops when the $SCR = 1$. (a): PSC loop gain is 390, (b): PSC loop gain is 200, (c) PSC loop gain is 50. The dynamics are initiated by a step change in the power order P_1^{ref}.

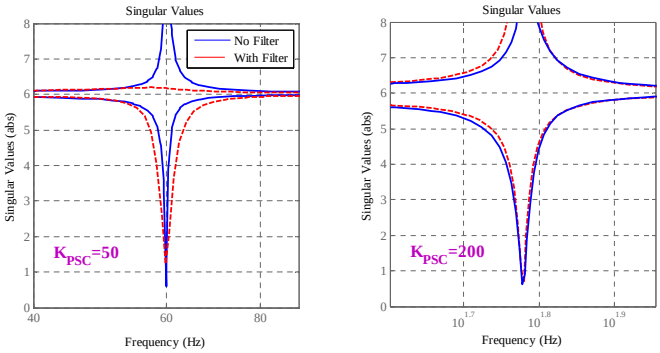

Fig. 18: Effects of high-pass filter and large gain.

the gain is increased from 50 to 200, the minimum singular value becomes less than 1. The MIMO system analysis results corroborate with the analysis results concluded from the power and angle transfer function analysis and simulation.

V. Conclusion

Stability analysis of the VSC-HVDC system connected to a very weak ac system has been presented in this study. Three different controls for VSC are considered including a power synchronization control, a vector control with PI outer loops, and a vector control with simple power control. The impedance-based analysis is implemented to derive the converter input impedance considering the detailed controls. The derived impedance model is then used to investigate the interactions between the converter and the weak ac grid. The MIMO system analysis is utilized to evaluate the system stability under several control strategies and operating conditions. The case studies show that the PSC is capable to handle higher power transfers compared to the vector controls. Moreover, the 60 Hz resonance stability of PSC is greatly improved by a high-pass filter. The PSC gain has a limit.

The overall results of the simulation and analysis demonstrate the superior performance of PSC in terms of power transfer when the ac grid is weak.

ACKNOWLEDGEMENT

The authors would like to acknowledge the help from Prof. Lingling Fan. The authors also wish to acknowledge anonymous reviewers whose comments helped improve this paper.

APPENDIX A
SYSTEM AND CONTROLLER PARAMETERS

This section provides the parameters of the system and controllers.

TABLE I: System Parameters of VSC-HVDC Model

Quantity	Value
ac system line voltage	100 kV
ac system frequency	60 Hz
base power	100 MW
dc rated voltage	180 kV
dc cable parameters	0.0139 Ω/km, 0.159 mH/km, 0.231 μF/km
dc cable length	20 km

TABLE II: Parameters of Individual VSC

Switching frequency	1620 Hz
Grid filter	0.048 H (for SCR 3)
Grid filter	0.088 H (for SCR 2)
Grid filter	0.25 H (for SCR 1)
dc capacitor	96 μF

TABLE III: Parameters of Power Synchronization

PSC controller	$k_{i,\|rmPSC}$=5
PI controller	k_{pv}=0.5, k_{iv}=10

TABLE IV: Parameters of Vector Controllers

	parameters	bandwidth (rad/s)
Current controller	k_p=50, k_i=100	1250
Alternating voltage controller	k_p=0.01, k_i=100	100 (SCR=1) 50 (SCR =2) 33 (SCR=3)
Outer PI controller	k_p=0.1, k_i=5	50

APPENDIX B
VECTOR CONTROL AND BANDWIDTHS

The inner current controls for the vector control should be designed to be much faster than the outer control loops. The converter voltage in abc frame is notated as v_{abc} and the current is notated as i_{abc}. The voltage at the point of the common coupling (PCC) is notated as v_1. An RL circuit is considered between the converter and the PCC. Therefore:

$$L\frac{d\overrightarrow{i}}{dt} + R\overrightarrow{i} = \overrightarrow{v} - \overrightarrow{v}_1. \tag{21}$$

where $\rightarrow$ is the space vector. The dq-reference frame is now utilized. It is assumed that the d-axis is aligned with the space vector of the PCC voltage, thus:

$$L\frac{d(i_d + ji_q)}{dt} + j\omega L(i_d + ji_q) + R(i_d + ji_q) = v_d + jv_q - v_{1d}. \tag{22}$$

Separating equation (22) into dq-axes, the plant model for the current control design is derived:

$$L\frac{di_d}{dt} + Ri_d = \underbrace{v_d - v_{1d} + \omega Li_q}_{u_d} \tag{23}$$

$$L\frac{di_q}{dt} + Ri_q = \underbrace{v_q - \omega Li_d}_{u_q} \tag{24}$$

The plant model for the current controller is assumed as $1/(R+sL)$ for both d and q axes. The inputs are u_d, u_q, while the outputs are i_d and i_q. The feedback controls are designed for the dq-axis to track the reference currents. In addition, to generate the dq components of the converter voltage, the cross coupling and feed-forward voltage terms should be added to the design.

A simplified inner current control block is illustrated in Fig. 19. The loop gain of system is represented by:

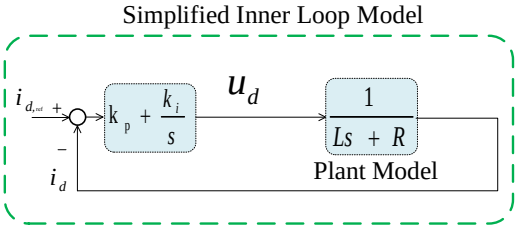

Fig. 19: Simplified block diagram for inner loop control.

$$l(s) = \frac{k_p}{Ls}\left(\frac{s + \frac{k_i}{k_p}}{s + \frac{R}{L}}\right). \tag{25}$$

As it is mentioned in [10], the plant pole is fairly close to the origin. Therefore, this plant pole is canceled by the compensator zero and the loop gain becomes:

$$l(s) = \frac{k_p}{Ls} \tag{26}$$

The closed-loop transfer function can be represented as:

$$G_{\text{Inner}}(s) = \frac{l(s)}{1 + l(s)} = \frac{1}{\tau s + 1} \tag{27}$$

where $\tau = \frac{L}{k_p}$ and $k_i = \frac{R}{\tau}$.

The inner loop gains are designed so that the bandwidth of the inner loop with $k_p = 50$, $k_i = 100$, and $L = 0.04H$ is around 1250 rad/s.

Compared to the inner current controller, the outer loop is designed to be very slow to reflect the dynamic changes. The simplified block diagram of the outer control loop is illustrated in Fig. 20. As the dq-reference frame is aligned with the PCC voltage, the real and reactive powers can be expressed as $P = V_1 i_d$ and $Q = V_1 i_q$, where, V_1 is the magnitude of PCC voltage.

A closed-loop simplified transfer function is represented as:

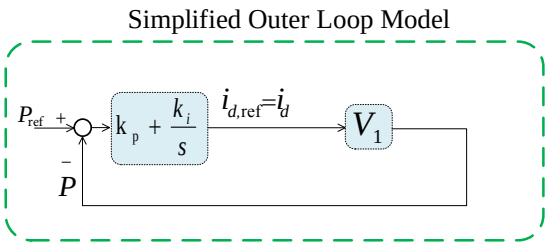

Fig. 20: Simplified block diagram for outer loop control.

$$G_{\text{outer}}(s) = \frac{\left(k_p + \frac{k_i}{s}\right) V_1}{1 + \left(k_p + \frac{k_i}{s}\right) V_1} = \frac{\frac{k_p}{k_i} s + 1}{\left(\frac{1}{V_1 k_i} + \frac{k_p}{k_i}\right) s + 1} \quad (28)$$

This is a first-order transfer function to the form of $\frac{as+1}{\tau s+1}$, where τ is the time constant ($\tau = \left(\frac{1}{V_1 k_i} + \frac{k_p}{k_i}\right)$) and the system bandwidth can be found as $1/\tau$. In this study, the outer loop gains are designed so that the bandwidth of the outer loop with $k_p = 0.1$ and $k_i = 5$ is 4 rad/s. This bandwidth is 300 times slower than the inner control bandwidth.

The ac voltage PI controller is designed based on $\Delta Q = V_1 \Delta i_q$, where V_1 is the PCC voltage. Furthermore, the PCC voltage change ΔV_1 is proportional to ΔQ. Hence, the plant model is derived as:

$$\Delta V_1 = \frac{\Delta Q}{SCR} = \frac{V_1}{SCR} \Delta i_q \quad (29)$$

The closed-loop system transfer function can be computed as:

$$\frac{\Delta V_1}{\Delta V_1^{\text{ref}}} = \frac{k_p s/k_i + 1}{(k_p + SCR)s/k_i + 1} \quad (30)$$

with the assumption that V_1 is approximately 1 pu. Therefore, the time constant and the bandwidth are as follows:

$$\tau = \frac{k_p + SCR}{k_i} \quad (31)$$

$$\omega_{bw} = 1/\tau \quad (32)$$

For $k_p = 0.01$, $k_i = 100$ and $SCR = 1$, the bandwidth is 100 rad/s. For $SCR = 2$, the bandwidth is 50 rad/s.

Appendix C
Derivation of Impedance Matrix for Vector Control

The dynamics of the inner current controller can be expressed as:

$$\bar{V}_c^c = -\left(k_p + \frac{k_i}{s}\right)(\bar{I}_{\text{ref}}^c - \bar{I}_1^c) - j\omega L \bar{I}_1^c + \frac{1}{s\tau + 1} \bar{V}_1^c \quad (33)$$

where superscript c denotes the converter $d-q$ frame, $\bar{V}_1^c$ is the PCC voltage converted to dq frame, and I_1 is the converter dq frame current obtained from I_{1abc}. It is noted that a first order filter is also included in the design and τ is the time constant of the filter (0.001). Rearranging (33) and separating it to $d-q$ components [6]:

$$\boldsymbol{I}_1^c = \underbrace{\begin{bmatrix} g_c(s) & 0 \\ 0 & g_c(s) \end{bmatrix}}_{G_c(s)} \boldsymbol{I}_{\text{ref}}^c + \underbrace{\begin{bmatrix} y_i(s) & 0 \\ 0 & y_i(s) \end{bmatrix}}_{Y_i(s)} \boldsymbol{V}_1^c \quad (34)$$

where $\boldsymbol{I}_1^c$, $\boldsymbol{I}_{\text{ref}}^c$ and $\boldsymbol{V}_1^c$ are vectors of $d-$axis and $q-$axis variables in converter $d-q$ frame.

$$\begin{cases} g_c(s) &= \frac{k_p s + k_i}{Ls^2 + k_p s + k_i} \\ y_i(s) &= \frac{s^2}{(Ls^2 + k_p s + k_i)(s\tau + 1)} \end{cases} \quad (35)$$

Now, impedance of the vector controlled converter can be derived if $\boldsymbol{I}_{\text{ref}}$ can be expressed by voltage and current vectors in the grid $d-q$ frame. The PLL is in charge of converting the components from the converter $d-q$ frame to the grid $d-q$ frame by synchronizing the angle. In the next subsections, the effect of outer loops and the PLL will be added to derive the impedance model of the vector controlled converter. Applying the small signal analysis to (34) will result in:

$$\Delta \boldsymbol{I}_1^c = \underbrace{\begin{bmatrix} g_c(s) & 0 \\ 0 & g_c(s) \end{bmatrix}}_{G_c(s)} \Delta \boldsymbol{I}_{\text{ref}}^c + \underbrace{\begin{bmatrix} y_i(s) & 0 \\ 0 & y_i(s) \end{bmatrix}}_{Y_i(s)} \Delta \boldsymbol{V}_1^c \quad (36)$$

A. Effect of Outer Loops

Outer PI outer loops are illustrated in Fig. 1, where the d axis will control the active power and q axis is in charge of the converter input voltage. The primary dynamic equations of the PI outer loops for deriving the reference $d-q$ axis current can be expressed as:

$$\begin{cases} I_{d,\text{ref}}^c &= (P_{\text{ref}} - P) F_{PI} \\ I_{q,\text{ref}}^c &= (V_{\text{ref}} - V_1) F_{VI} \end{cases} \quad (37)$$

Where V_1 is the magnitude of the PCC voltage, V_{ref} is the reference magnitude of the PCC voltage, F_{PI} is the PI controller transfer function ($k_{pp} + \frac{k_{ip}}{s}$) for power control loop and, F_{VI} is the PI controller transfer function ($k_{pv} + \frac{k_{iv}}{s}$) to track the PCC voltage magnitude. Applying the small signal analysis to (37):

$$\begin{cases} \Delta I_{d,\text{ref}}^c &= -F_{PI} \Delta P \\ \Delta I_{q,\text{ref}}^c &= -F_{VI} \Delta V_1 \end{cases} \quad (38)$$

The magnitude of the PCC voltage can be derived by: $V_1 = \sqrt{V_{1d}^2 + V_{1q}^2}$, and the converter output active power can simply be derived by: $P = V_{1d} I_{1d} + V_{1q} I_{1q}$, therefore, applying small signal analysis:

$$\Delta P = I_{1d0} \Delta V_{1d} + V_{1d0} \Delta I_{1d} + I_{1q0} \Delta V_{1q} + V_{1q0} \Delta I_{1q} \quad (39)$$

$$\begin{aligned} \Delta V_1 &= \frac{V_{1d0} \Delta V_{1d} + V_{1q0} \Delta V_{1q}}{\sqrt{V_{1d0}^2 + V_{1q0}^2}} \\ &= \frac{V_{d0}}{V_0} \Delta V_{1d} + \frac{V_{q0}}{V_0} \Delta V_{1q} \end{aligned} \quad (40)$$

By replacing the (39) and (40) into (38):

$$\Delta \boldsymbol{I}^c_{\text{ref}} = \underbrace{\begin{bmatrix} -F_{PI}v_{1d0} & -F_{PI}v_{1q0} \\ 0 & 0 \end{bmatrix}}_{G_1(s)} \Delta \boldsymbol{I}^c_1 + \underbrace{\begin{bmatrix} -F_{PI}I_{d0} & -F_{PI}I_{q0} \\ -\frac{V_{d0}}{V_0}F_{VI} & -\frac{V_{q0}}{V_0}F_{VI} \end{bmatrix}}_{G_2(s)} \Delta \boldsymbol{V}^c_1 \quad (41)$$

The impedance of the vector controlled converter with outer loops and without the PLL is then derived by substituting (41) into (36):

$$\Delta \boldsymbol{I}^c_1 = \underbrace{\frac{G_e(s)G_2(s) + Y_i(s)}{I - G_e(s)G_1(s)}}_{\left[Z^c_{Rec}\right]^{-1}} \Delta \boldsymbol{V}^c_1 \quad (42)$$

B. The PLL Effect

Impedance analysis of the PLL has been performed in [6] in detail. The final equations are adopted here and detailed analysis can be found in [6]. The main goal is to convert the $\bar{I}^c_1$ and $\bar{V}^c_1$ from the converter frame to the grid frame components ($\bar{I}_1$ and $\bar{V}_1$) by :

$$\Delta \boldsymbol{I}^c_1 = \Delta \boldsymbol{I}_1 - \underbrace{\begin{bmatrix} 0 & \frac{Q_0}{V_0}G_{PLL} \\ 0 & \frac{Q_0}{V_0}G_{PLL} \end{bmatrix}}_{Gp_{PLL}} \Delta \boldsymbol{V}_1$$

$$\Delta \boldsymbol{V}^c_1 = \underbrace{\begin{bmatrix} 1 & 0 \\ 0 & 1 - V_{10}G_{PLL} \end{bmatrix}}_{Gs_{PLL}} \Delta \boldsymbol{V}_1 \quad (43)$$

where G_{PLL} is a simple PI controller as:$G_{PLL} = K_p^{PLL} + \frac{k_i^{PLL}}{s}$. For deriving the impedance model of the vector controlled converter with the outer power loop and the PLL effect, (43) is substituted into (42), then the result will be:

$$Z_{Rec}(s) = \frac{1}{Gp_{PLL} + \left[Z^c_{Rec}\right]^{-1} Gs_{PLL}} \quad (44)$$

REFERENCES

[1] O. B. Nayak, A. Gole, D. Chapman, and J. Davies, "Dynamic performance of static and synchronous compensators at an HVDC inverter bus in a very weak ac system," *IEEE Trans. Power Syst.*, vol. 9, no. 3, pp. 1350–1358, 1994.

[2] X. Koutiva, T. Vrionis, N. Vovos, and G. B. Giannakopoulos, "Optimal integration of an offshore wind farm to a weak ac grid," *IEEE Trans. Power Del.*, vol. 21, no. 2, pp. 987–994, 2006.

[3] J. Pan, R. Nuqui, K. Srivastava, T. Jonsson, P. Holmberg, and Y.-J. Hafner, "Ac grid with embedded vsc-hvdc for secure and efficient power delivery," in *Energy 2030 Conference, IEEE*, Nov 2008, pp. 1–6.

[4] A. Gavrilovic, "Ac/dc system strength as indicated by short circuit ratios," in *International Conference on AC and DC Power Transmission*, Sep 1991, pp. 27–32.

[5] X. Zheng, "Characteristics of HVDC connected to weak ac systems part1: HVDC transmission capability," *Power System Technology*, vol. 21, no. 1, pp. 12–16, 1997.

[6] L. Harnefors, M. Bongiorno, and S. Lundberg, "Input-admittance calculation and shaping for controlled voltage-source converters," *IEEE Trans. Ind. Electron.*, vol. 54, no. 6, pp. 3323–3334, 2007.

[7] F. Schettler, H. Huang, and N. Christl, "HVDC transmission systems using voltage sourced converters design and applications," in *IEEE Power Engineering Society Summer Meeting*, vol. 2, 2000, pp. 715–720.

[8] N. Flourentzou, V. G. Agelidis, and G. D. Demetriades, "VSC-based HVDC power transmission systems: An overview," *IEEE Trans. Power Electron.*, vol. 24, no. 3, pp. 592–602, 2009.

[9] L. Zhang, L. Harnefors, and H.-P. Nee, "Modeling and control of VSC-HVDC links connected to island systems," *IEEE Trans. Power Syst.*, vol. 26, no. 2, pp. 783–793, 2011.

[10] A. Yazdani and R. Iravani, *Voltage-sourced converters in power systems: modeling, control, and applications*. John Wiley & Sons, 2010.

[11] S. Li, T. Haskew, and L. Xu, "Control of HVDC light system using conventional and direct current vector control approaches," *IEEE Trans. Power Electron.*, vol. 25, no. 12, pp. 3106–3118, 2010.

[12] M. Durrant, H. Werner, and K. Abbott, "Model of a VSC-HVDC terminal attached to a weak ac system," in *IEEE Conference on Control Applications.*, vol. 1, 2003, pp. 178–182.

[13] L. Zhang, L. Harnefors, and H.-P. Nee, "Power-synchronization control of grid-connected voltage-source converters," *IEEE Trans. Power Syst.*, vol. 25, no. 2, pp. 809–820, 2010.

[14] L. Xu and L. Fan, "Impedance-based resonance analysis in a VSC-HVDC system," *IEEE Trans. Power Del.*, vol. 28, no. 4, pp. 2209–2216, 2013.

[15] A. Egea-Alvarez, S. Fekriasl, F. Hassan, and O. Gomis-Bellmunt, "Advanced vector control for voltage source converters connected to weak grids," *IEEE Trans. Power Syst.*, vol. 30, no. 6, pp. 3072–3081, 2015.

[16] L. Zhang, L. Harnefors, and H.-P. Nee, "Interconnection of two very weak ac systems by VSC-HVDC links using power-synchronization control," *IEEE Trans. Power Syst.*, vol. 26, no. 1, pp. 344–355, 2011.

[17] P. Mitra, L. Zhang, and L. Harnefors, "Offshore wind integration to a weak grid by VSC-HVDC links using power-synchronization control: A case study," *IEEE Trans. Power Del*, vol. 29, no. 1, pp. 453–461, 2014.

[18] L. Zhang, H.-P. Nee, and L. Harnefors, "Analysis of stability limitations of a VSC-HVDC link using power-synchronization control," *IEEE Trans. Power Syst.*, vol. 26, no. 3, pp. 1326–1337, 2011.

[19] K. M. Alawasa and Y. A.-R. Mohamed, "Impedance and damping characteristics of grid-connected vscs with power synchronization control strategy," *IEEE Trans. Power Syst.*, vol. 30, no. 2, pp. 952–961, 2015.

[20] J. Sun, "Impedance-based stability criterion for grid-connected inverters," *IEEE Trans. Power Electron.*, vol. 26, no. 11, pp. 3075–3078, 2011.

[21] Z. Miao, "Impedance-model-based SSR analysis for type 3 wind generator and series-compensated network," *IEEE Trans. Energy Convers.*, vol. 27, no. 4, pp. 984–991, 2012.

[22] L. Xu, L. Fan, and Z. Miao, "Dc impedance-model-based resonance analysis of a VSC-HVDC system," *IEEE Trans. Power Del.*, vol. 30, no. 3, 2015.

[23] B. Wen, D. Boroyevich, R. Burgos, P. Mattavelli, and Z. Shen, "Small-signal stability analysis of three-phase ac systems in the presence of constant power loads based on measured dq frame impedances," *IEEE Trans. Power Electron.*, no. 10, pp. 5952–5963, Oct. 2015.

[24] M. Morari and E. Zafiriou, *Robust process control*. Morari, 1989.

[25] N. Lehtomaki, N. R. Sandell Jr, M. Athans *et al.*, "Robustness results in linear-quadratic gaussian based multivariable control designs," *Automatic Control, IEEE Transactions on*, vol. 26, no. 1, pp. 75–93, 1981.

[26] L. Piyasinghe, Z. Miao, J. Khazaei, and L. Fan, "Impedance model-based SSR analysis for TCSC compensated type-3 wind energy delivery systems," *IEEE Trans. Sustain. Energy.*, vol. 6, no. 1, pp. 179–187, 2015.

Javad Khazaei (S'10 M'16) received his Bachelors degree in Electrical Engineering from Mazandaran University (2009) and Masters degree from Urmia University (2011) in Iran. He received his Ph.D degree at University of South Florida (USF) in Summer 2016. He is currently an Assistnat Professor at Penn State Harrisburg. His research interests include Microgrid modeling, Renewable Energy Integration, and Power Electronics applications.

Zhixin Miao (S'00 M'03 SM'09) is with the University of South Florida (USF), Tampa. Prior to joining USF in 2009, he was with the Transmission Asset Management Department with Midwest ISO, St. Paul, MN, from 2002 to 2009. His research interests include power system stability, microgrid, and renewable energy.

Lakshan Piyasinghe is a recent Ph.D. graduate from USF SPS lab. He received his Bachelor degree in Electrical Engineering in 2006 from University of Moratuwa, Sri Lanka. He started his Ph.D. study at USF in Fall 2010 and his research interests include dynamic modeling and analysis of power electronic systems and power systems.